Structures of yeast mitochondrial ADP/ATP carriers support a domain-based alternating-access transport mechanism

Jonathan J. Ruprecht[a], Alex M. Hellawell[a], Marilyn Harding[a], Paul G. Crichton[a],
Airlie J. McCoy[b] and Edmund R.S. Kunji[a,1]

Supplementary Information

Note S1: Inhibitor binding site

Density maps for all structures after molecular replacement ($2mF_o$-DF_c and mF_o-DF_c maps, CATR excluded from the search model) showed extra density within the protein cavity, attributable to the inhibitor CATR, which could be modelled into the density (Fig. S2). We have modelled CATR with a β-D-glucoside ring, rather than the α-D-glucoside originally modelled in the structures of bovine AAC1 (1, 2). A β-D-glucoside ring is consistent with the X-ray crystal structure of atractyloside, and with a remodelling of CATR in the bovine AAC1 $P2_12_12$ structure (3). The change in anomer of the glucoside ring does not significantly alter the interactions of CATR with binding-site residues in bovine AAC1 (see Table S3).

The new structures show that CATR binds to Aac2p and Aac3p in a similar manner to the bovine AAC1 structures. CATR is bound deep within the cavity, displaced from the three-fold pseudo-symmetry axis, with the diterpenoid moiety towards the matrix side. The inhibitor is bound by multiple salt bridge and hydrogen bond interactions. The nature of these interactions differs slightly depending on the crystal form (see Table S3). The two sulfate groups form salt bridges to Arg and Lys residues. Aac2p forms interactions from Arg204 to sulfate oxygen atom O10 (3.1-3.3 Å distance, depending on the crystal form), and from Lys108 to sulfate oxygen atoms O10 (2.9-3.4 Å distance) and O15 (2.7-3.1 Å distance). Aac3p shows salt-bridge interactions from the equivalent residues Arg193 and Lys97 to the sulfate groups. The interaction distances vary in the four Aac3p molecules observed in the crystal structures (two molecules in the asymmetric unit for both $P2_12_12_1$ and $P2_1$ crystal forms), due to subtle differences in the binding-pocket of these molecules. Nevertheless, these salt-bridges clearly contribute significantly to the binding-affinity of CATR for the protein. An additional salt bridge, observed in all the crystal structures, is formed between one of the carboxyl groups of CATR (oxygen atoms O3 and O4) and Arg96 (Aac2p) or Arg85 (Aac3p). This carboxyl group is the only chemical difference between ATR and CATR, and the salt bridge it forms with the protein is responsible for the higher binding affinity of CATR for ADP/ATP carriers. This assignment is in agreement with NMR studies performed on derivatives of atractylosides (4, 5) and the X-ray structure of atractyloside (3). The interaction of this carboxyl group with Arg96 led to the differences observed in the unfolding patterns of ATR and CATR inhibited Aac3p in atomic force microscopy studies (5). Arg96 is the residue mutated in the op_1 mutant (6), and is also implicated in substrate binding (2, 7).

Additional hydrogen bonds contribute to binding of the inhibitor. The hydroxyl group of the diterpenoid moiety forms a hydrogen bond to Arg252 in Aac2p (Arg241 in Aac3p). The Aac3p structures, and molecule B in the Aac2p $P2_12_12_1$ crystal form, reveal a hydrogen bond between Asn104 (Aac2p; Asn93 in Aac3p) and sulfate oxygen O15. A similar hydrogen bond is seen in the $P2_12_12$ bovine AAC1 structure. In the $C222_1$ Aac2p and bovine AAC1 structures, the equivalent Asn residue is positioned slightly further from the sulfate group. In molecule A of the Aac2p $P2_12_12_1$ structure, Asn104 adopts a different rotamer, positioning it too far away to form a hydrogen bond with CATR. There is a possible weak hydrogen bond from Arg204 (Aac2p; Arg193 in Aac3p) to the hydroxymethyl group of CATR (3.5 Å distance). However, this interaction is unlikely to contribute significantly to binding affinity, since succinyl-ATR, a derivative in which a succinyl group is attached to the hydroxymethyl group of ATR, is a high affinity inhibitor of ADP/ATP carriers from rat liver (8). Succinyl-ATR is probably accommodated within the binding site by a rotation of the hydroxymethyl group. The isovaleric group is not involved in salt bridge or hydrogen bond interactions, but is involved in hydrophobic contacts.

Note S2: Aac2p and Aac3p are monomeric

The oligomeric state of a protein can be crucial to understanding how it functions. Early biochemical and biophysical experiments suggested that mitochondrial carriers were dimeric, but recent data indicate that mitochondrial carriers are monomeric in structure and function (9). Native oligomers are often retained in purification and crystallization (10-12). An AAC1 dimer was observed in the *C*222$_1$ crystal form (1) (Fig. S3*H*), and postulated to represent a functional dimer. However, the interactions are mediated principally by cardiolipin molecules, and the surface area is less than 500 Å^2 and may simply represent crystal contacts.

The Aac2p and Aac3p crystals are composed of stacked 2D sheets of protein molecules. Molecules within the 2D sheets are oriented with their three-fold pseudo-symmetry axis almost perpendicular to the sheet, similar to their orientation within the membrane. Similar packing has been observed in the bovine AAC1 crystals (1). The *P*2$_1$2$_1$2$_1$ Aac2p crystal and both *P*2$_1$ and *P*2$_1$2$_1$2$_1$ Aac3p crystals have two molecules in the asymmetric unit, and the crystals show closer interactions between monomers than the bovine *C*222$_1$ crystal structure. We therefore investigated our crystals for a consistent dimerization interface. Analysis of protein-protein interactions from crystal structures is complicated by the fact that molecules are brought into close contact by crystal packing. To be classified as a native dimer, two neighbouring carriers would have to meet several criteria: (a) they should be in the same orientation, (b) they should bury a significant surface area upon dimerization, (c) interactions should be discriminatory since they must exclude other carriers with similar structures but different functions, (d) there should not be a significant tilt of the 3-fold pseudo-symmetry axis of each monomer with respect to the membrane plane. Possible interfaces between monomers in the fungal ADP/ATP carrier crystals are shown in Figure S3. The two molecules in the asymmetric unit of the *P*2$_1$2$_1$2$_1$ Aac3p crystals are in opposite orientations, and therefore cannot represent a native dimer. However, within the unit cell there is one arrangement of nearest neighbours with the same orientation (Fig. S3*A*). There are three possible candidates in the *P*2$_1$ Aac3p crystal (Fig. S3*B* to *D*), two in the *P*2$_1$2$_1$2$_1$ Aac2p crystal (Fig. S3*E* and *F*), and one in the *C*222$_1$ Aac2p crystal (Fig. S3*G*). Of these candidates, *A*, *B* and *F* show a tilt of the 3-fold pseudo-symmetry axis with respect to the membrane plane, making them unlikely candidates for a native dimer (although crystal contacts could perturb the interface). In all cases, the interface area is low (<850 Å^2 per monomer), and is less than 6% of the total surface area of a monomer. Cardiolipin molecules sit between the monomers for 6 of the 7 identified interfaces, and contribute to 20-80% of the interface area. However, the relatively non-specific nature of lipid-protein interactions makes them unlikely candidates for forming a key component of a functional dimer interface (9). Interfaces *C*, *E* and *G* are similar and represent preferred packing seen in both Aac2p and Aac3p. This interface includes a lysine-glycine hydrogen bond, which involves the backbone carbonyl of glycine, and thus is unlikely to confer functionality on the interface. This interface is not observed in the Aac3p $P2_12_12_1$ or AAC1 $C222_1$ crystal forms. Thus, no consistent interface is found for all carriers for which there is structural information. The lack of a dimerization interface is consistent with earlier work showing that Aac2p and Aac3p are monomeric in detergent solution (13), and that Aac2p functions as a monomer in the mitochondrial membrane (14).

Methods

Construction of yeast expression strains

The Aac3p construct was prepared as described previously (15). The Aac2p construct was derived from the *S. cerevisiae AAC2* gene, with an N-terminal $(His)_8$ tag and Factor Xa cleavage site upstream of residues 16-318 of Aac2p. The modified gene was cloned into a modified pYES3 vector, under the control of the promoter for the *S. cerevisiae* phosphate carrier *PIC2*, and checked by sequencing (Source Bioscience).

Using standard techniques, expression vectors were transformed into *S. cerevisiae* strain WB12 (MAT*α ade2-1 trp1-1 ura3-1 can1-100 aac1::LEU2 aac2::HIS3*) (16), which lacks functional Aac1p and Aac2p carriers. Transformants were selected initially on SC medium minus Trp plates, and then on YEPG plates, confirming that they were expressing functional ADP/ATP carriers.

Expression, preparation of mitochondria and protein purification

For Aac2p, a two litre preculture was used to inoculate 80 litres of YEPG medium in an Applikon 140 Pilot System with an eZ controller. Cells were grown at 30 °C, pH 5.0, dO_2 80%, and harvested at an OD_{600} of 9.5 by centrifugation at 4000*g* for 20 min. For Aac3p, a one litre preculture was used to inoculate 55 litres of YEPG medium in an Applikon ADI1075 fermenter with a 1030 controller. Cells were grown at 30 °C, pH 5.0, dO_2 80%, and harvested at an OD_{600} of 9-16 by centrifugation at 4000*g* for 20 min. Mitochondria were prepared using established methods (15), flash frozen in liquid nitrogen, and stored under liquid nitrogen until use.

Aac2p and Aac3p were purified as described previously (17), with the following modifications. Aac2p was solubilized in 2% (w/v) undecyl β-D-maltoside (Anagrade, Affymetrix), and exchanged into 5-cyclohexyl-1-pentyl-β-D-maltoside (Cymal-5, Anagrade, Affymetrix) whilst bound to the Ni Sepharose column. After Factor Xa cleavage, Aac2p was spun through a Vivapure Q Mini H spin column (Sartorius), and then dialyzed against 10 mM Tris pH 7.4, 50 mM NaCl, 0.2% (w/v) Cymal-5 for 4-5 h. The protein was harvested, and concentrated to 6-7 mg ml^{-1} using Amicon Ultra Centrifugal Filter Units (50,000 molecular weight cut-off). The protein concentration was determined using the BCA method (Pierce). Aac3p was solubilized in 2% (w/v) undecyl β-D-maltoside, and exchanged into n-decyl-β-D-maltoside (DM) (Anagrade, Affymetrix). After Factor Xa cleavage, residual protease was removed using Xarrest Agarose (EMD Millipore), and the protein was concentrated to 6-7 mg ml^{-1}. Following purification, protein was either used immediately in crystallization trials, or flash frozen and stored in liquid nitrogen.

Crystallization and data collection

Crystals were initially obtained of Aac3p, using an in-house systematic crystallization screen. The $P2_12_12_1$ crystal used for data collection was grown by sitting-drop vapour diffusion, mixing 200 nl of protein with 200 nl of precipitating solution containing 0.1 M Tris pH 8.5, 20 mM sodium citrate, 10% (v/v) t-butanol, 28% (v/v) PEG 400. Small plate-like crystals appeared at 17 °C within a few days, and were harvested after 14 days. Crystals were cryo-protected by soaking in precipitating solution containing 30% (v/v) PEG 400. $P2_1$ crystals grew under similar conditions. Many of these crystals showed streaky or split diffraction spots, probably due to pseudo-merohedral twinning, and were unsuitable for structure determination. Fortunately, one crystal did not show these defects. This crystal was grown using the sitting-drop vapour diffusion method, mixing 200 nl of protein with 200 nl of a precipitating solution containing 0.1 M Tris pH 8.5, 5 mM sodium citrate, 11% (v/v) t-butanol, 26% (v/v) PEG 400. Crystals appeared within a few days, and were harvested directly from the drops after one month. Crystals were harvested using Mitegen loops (Ithaca, NY, USA) and cryo-cooled by plunging into liquid nitrogen.

Crystals of Aac2p grew under similar conditions to those used for Aac3p. The $C222_1$ crystal used for structure determination was obtained using the sitting-drop vapour diffusion technique at 22 °C, mixing 2 μl of protein with 2 μl of precipitating solution (0.1 M Tris pH 8.5, 10 mM sodium citrate, 8% (v/v) t-butanol, 28% (v/v) PEG 600), and equilibrating over a reservoir containing 0.5 ml of precipitating solution. Protein was supplemented with 0.2% (w/v) n-nonyl-β-D-glucoside (NG) (Anagrade, Affymetrix) before drop setup. Crystals appeared within 24 h, reached their final size within about 48 h, and were harvested after 6 days. Cryo-protection was achieved by soaking the crystals in precipitant solution containing 32% (v/v) PEG 600. The $P2_12_12_1$ crystal was obtained from protein supplemented with a 1:1 (mol:mol) ratio of 1',3'-bis[1,2-dimyristoyl-*sn*-glycero-3-phosphate]-*sn*-glycerol (tetramyristoyl cardiolipin, Avanti Polar Lipids) prior to drop setup. The crystal was grown by sitting-drop vapour diffusion, mixing 200 nl of protein with 200 nl of precipitating solution (0.1 M Tris pH 8.5, 10 mM sodium citrate, 50 mM ammonium sulfate, 8% (v/v) t-butanol, 23.5% (v/v) PEG 600). Crystals were harvested after 5 days. The crystals were cryo-protected in precipitating solution containing 31% (v/v) PEG 600, harvested using Mitegen loops, and cryo-cooled by plunging into liquid nitrogen.

The small size of the crystals (typically 25-50 μm x 10-20 μm x <10 μm, although the $C222_1$ Aac2p crystals tended to be slightly larger) meant that screening and data collection were dependent on microfocused synchrotron X-ray beamlines. The datasets used for structure determination came from crystals collected at 100 K on the European Synchrotron Radiation Facility (ESRF) beamline ID23-2, using a 10-μm beam. Both Aac3p and the Aac2p $P2_12_12_1$ datasets were collected from two positions on their respective crystals. A helical data collection strategy was used to collect the Aac2p $C222_1$ dataset (18).

Intensities for the Aac2p $C222_1$ crystal were integrated using the program iMosflm (19) and merged using Scala from the CCP4 suite (20). The $C222_1$ crystals showed anisotropic diffraction and evidence of diffuse scattering. Intensities for the Aac2p $P2_12_12_1$, and the Aac3p $P2_12_12_1$ and $P2_1$ crystals, were integrated using XDS (21), and merged using Aimless (22). The programs Pointless (22, 23) and phenix.xtriage (24) were used to check data quality and space-group assignments. Data collection statistics are shown in Table S1.

Structure determination and refinement: Aac2p

Structure determination was initially carried out using a $C222_1$ crystal that diffracted to 3-Å resolution. Phases were determined by molecular replacement (MR) using the program Phaser (25), and the coordinates of the bovine ADP/ATP carrier ($P2_12_12$ crystal form, PDB code 1OKC) as a search model. Non-conserved side chains of 1OKC were pruned before MR, and non-protein atoms were omitted from the search model and initial phase calculation. A single unique MR solution was found (RFZ=9.3, TFZ=16.3, final LLG=218), with one molecule in the asymmetric unit. Density for the inhibitor CATR, not included in the search model, was visible in the maps calculated from the initial phases, giving confidence in the molecular replacement solution and quality of the phases. The maps revealed differences in the positions of several loops regions. Manual model building was performed using the program Coot (26), and refinement was performed with Refmac, initially using jelly-body restraints (27). At this stage, a dataset to 2.5 Å resolution was collected, and structure determination was continued against this dataset, retaining the original R_{free} reflection set. Refinement was continued with autoBUSTER with LSSR restraints (28).

Despite model building and refinement, it was not possible at this stage to decrease R_{free} below 37%. The data was reprocessed in the subgroups of $C222_1$, and analysis showed that the crystals were not twinned in these space-groups. The subgroup R_{free} sets incorporated the $C222_1$ symmetry to avoid bias. Refinement in the $P2_1$ space-group led to a 3-4% drop in R_{free}, and further model building was pursued in this space-group. Density maps revealed the position of lipids, interpreted as cardiolipin molecules. Refinement using Refmac with TLS parameterization (29) resulted in a model with R_{free} below 30%. TLS groups were determined using phenix.find_tls_groups, from the Phenix suite of programs (24). Since there were no significant coordinate differences between the two molecules in the $P2_1$ asymmetric unit, refinement was tested again in the $C222_1$ space-group. Using phenix.refine (30) with TLS, secondary structure restraints and optimization of stereochemistry and atomic displacement parameter weights, it was possible to refine the model in the $C222_1$ space-group to a final R=25.9%, R_{free}=29.7%. The final model consists of residues 24-309 of Aac2p, a CATR molecule, 3 cardiolipins, and one NG molecule. Residues 160-167 and 215-227 are unmodelled owing to poor density. The electron density maps for the $C222_1$ crystal form had poor density in some regions, for example in matrix helices h12 and h34 (see Fig. 1 for overviews of the structures). Structure determination using the $P2_12_12_1$ crystal form was therefore pursued.

Phases for the $P2_12_12_1$ crystal were determined using a preliminary model of Aac2p ($C222_1$ crystal form) as a MR search model. Data analysis with Phaser revealed the presence of translational non-crystallographic symmetry (NCS). Phaser found a single solution (RFZ=11.5, TFZ=18.9, final LLG=1725), with two molecules in the asymmetric unit. Initial refinement with Refmac, using jelly-body and local NCS restraints, revealed differences between the two molecules in the asymmetric unit. At this stage, $2m\mathrm{F_o}$-$D\mathrm{F_c}$ and $m\mathrm{F_o}$-$D\mathrm{F_c}$ maps showed density for CATR, lipid molecules, and unmodelled regions of the protein. Density for the cytoplasmic ends of helices 1 and 6, and for the matrix helices was better defined in these maps than in maps for the $C222_1$ crystal. Model building was performed in Coot, and refinement in phenix.refine with torsion-angle NCS restraints, secondary structure restraints, and optimization of stereochemistry and atomic displacement parameter weights. The final model was refined to R=24.9%, $\mathrm{R_{free}}$=28.0%. The asymmetric unit contains two Aac2p molecules (chain A with residues 21-318; chain B with residues 24-309), two CATR molecules, 6 cardiolipins and one molecule of cymal-5. Density is missing for chain A residues 160-166 and 216-227, and for chain B residues 161-165 and 216-227, and they are not included in the model. Final refinement statistics for both crystal forms are shown in Table S1.

Coordinates and restraints for CATR were generated using the Grade web server (http://grade.globalphasing.org), using the isomeric SMILES string from the International Union of Basic and Clinical Pharmacology Database (www.iuphar-db.org, ligand ID 4572), and edited using JLigand (31) to reflect the charges on the carboxylate and sulphate groups. Coordinates and restraints for NG and cardiolipin were obtained from the Refmac monomer library. The restraints for cardiolipin were edited in JLigand to correct the stereochemistry of the phosphatidyl residues (32).

Structure determination and refinement: Aac3p

Phases were initially determined for the $P2_12_12_1$ crystal by MR. A preliminary model of Aac2p in the $C222_1$ crystal form, with non-conserved residues pruned to the gamma atom, was used as a search model. Phaser found a single solution, with two molecules in the asymmetric unit (RFZ=7.6, TFZ=7.2; RFZ=6.8, TFZ=23.7; final LLG=807). Refinement was then performed using jelly-body restraints in Refmac, and local NCS restraints (27), revealing subtle differences between the NCS-related molecules. The density maps revealed the position of CATR and three cardiolipin molecules per Aac3p monomer. Manual model building was carried out in Coot, and phenix.refine was used for refinement, using torsion-angle NCS restraints, secondary structure restraints, and optimization of stereochemistry and atomic displacement parameter weights. The model was refined to R=25.0%, R_{free}=29.7%. The asymmetric unit contains two Aac3p molecules (chain A with residues 13-304; chain B with residues 12-306), two CATR molecules and 6 cardiolipins. Density was missing for chain A residues 151-155 and 205-219, and for chain B residues 152-155 and 204-219, and they are excluded from the model.

Analysis of the $P2_1$ dataset by Phaser revealed the presence of translational NCS, and showed that the crystal was untwinned. Initial phases were determined by MR using the $P2_12_12_1$ Aac3p model as a search model. Phaser found a single solution with two molecules in the asymmetric unit (RFZ=18.2, TFZ=18.0, final LLG=1406). Initial refinement was performed using Refmac with jelly-body restraints. The resulting $2mF_o$-DF_c and mF_o-DF_c maps showed density for CATR, lipid molecules, and an extended helical N-terminus. Model building was performed in Coot, and further refinement in phenix.refine, using torsion-angle NCS restraints, secondary structure restraints, and optimization of stereochemistry and atomic displacement parameter weights. The model was refined to R=25.8%, R_{free}=29.5%. The asymmetric unit contains two Aac3p molecules (chain A with residues 4-304; chain B with residues 3-306), two CATR molecules and 6 cardiolipins. Density was missing for chain A residues 151-155 and 207-215, and for chain B residues 149-155 and 208-214, and they are excluded from the model. Final refinement statistics for both crystal forms are shown in Table S1. Figures were generated using Pymol (www.pymol.org).

Site-directed mutagenesis

Genes were amplified for polymerase chain reaction (PCR) by using KOD HotStart polymerase (Novagen) following the instructions of the manufacturer. Site-directed mutations in the structural gene of *aac*2 in the pYES-P*aac2*-*AAC2* vector (14) were introduced by using the overlap-extension PCR-based method (33) or the

Quikchange II site-directed mutagenesis kit (Stratagene). For the introduction of multiple mutations several rounds of site-directed mutagenesis were performed. For optimal expression in *Lactococcus lactis* residues 2-19 of the wild-type and mutant genes were removed by PCR and the resulting genes were cloned into the expression vector pNZ8048 under the control of a nisin A-inducible promoter (34, 35). The plasmid was transformed in *L. lactis* strain NZ9000 by electroporation, as described (35).

Growth of L. lactis and isolation of membranes

Precultures of *L. lactis* were obtained by inoculating M17 medium supplemented with 1% (w/v) glucose and 5 μg·ml^{-1} chloramphenicol from glycerol stocks and by incubating the cultures overnight at 30 ˚C with no aeration. The OD_{600} was measured and the cells were diluted to a starting OD_{600} of 0.1 in fresh M17 medium. Cells were grown at 30 ˚C with no aeration until the OD_{600} reached 0.5-0.7 and the expression of the recombinant proteins were induced by addition of nisin A with a dilution of 1:10,000 of spent M17 medium from nisin A excreting *L. lactis* strain NZ9700. The cells were grown for a further 3 h at 30 ˚C and then transferred to 20 ˚C for overnight incubation. Cells were harvested by centrifugation at 6,000*g* for 10 min at 4 ˚C (Sorvall), resuspended in 50 mM piperazine-N,N'-bis(ethanesulfonic acid, 100 mM NaCl, pH 7.0 (PIPES buffer) and collected by centrifugation as before. The cells were resuspended in 50 ml PIPES buffer and disrupted mechanically with a cell disruptor (Constant Cell Disruption Systems) in one pass at 30,000 psi. Whole cells and large debris were removed by centrifugation at 10,800*g* for 10 min at 4 ˚C and then at 20,400*g* for 10 min at 4 ˚C (in the case of 2 l large scale cultures) (Sorvall). Membranes were collected by ultracentrifugation at 138,000*g* for 40 min at 4 ˚C, washed and resuspended in PIPES buffer, and the centrifugation step was repeated. Pellets were resuspended in PIPES buffer to a total protein concentration of approximately 5 mg·ml^{-1} and stored in liquid nitrogen for transport assays.

Membrane vesicle fusions and transport assays

E. coli polar lipid extract and egg yolk phosphatidylcholine (both 20 mg·ml^{-1} in chloroform) were mixed in the mass ratio of 3:1 in a glass tube. The chloroform was evaporated by nitrogen while shaking and the lipids were resuspended in PIPES buffer with a homogenizer and frozen in liquid nitrogen.

Isolated membranes from *L. lactis* and a stock of liposomes were thawed from liquid nitrogen to room temperature (21°C). Fusion resuspensions were made by mixing membranes (1 mg of total protein), 5 mg liposomes, and 5 mM ADP pH 7.0 (from 10× stock) and by adding PIPES buffer to make a total volume of 1 ml. The membranes and liposomes were fused by seven cycles of freezing in liquid nitrogen and thawing at room temperature before storage in liquid nitrogen.

Membrane vesicle fusions were thawed and extruded 11 times using a 1-µm polycarbonate filter (Avanti Polar Lipids). The fused membranes were collected by ultracentrifugation at 300,000*g* for 30 min at 4 °C, resuspended in PIPES with 5 mM ADP and passed over a Poly-Prep Chromatography column (Bio-Rad) with G50 size exclusion beads, eluting in 1 ml PIPES buffer.

Transport of ^{14}C-labeled ADP was started by adding 100 µl fused membranes to 300 µl PIPES buffer with 1.34 µM ^{14}C-ADP (2.22 GBq·mmol^{-1}) at 30 ˚C. The transport was stopped at 15 s, 30 s, 45 s, 1 min, 2 min, 4 min and 6 min by the addition of 2 ml of cold PIPES buffer and filtering of membrane/liposome fusions onto a 0.45 µm cellulose nitrate filter, by using a vacuum manifold, with an additional washing step with 2 ml cold PIPES buffer. Levels of radioactivity accumulated in the fused membranes were quantified by transferring the filter into 3 ml Ultima Gold AB liquid scintillant (Packard Biosciences, Perkin Elmer) in a scintillation vial and by quantifying the amount of radioactivity with a liquid scintillation counter (Perkin Elmer). The initial rates were determined from the linear part of the uptake curves.

1. Nury H*, et al.* (2005) Structural basis for lipid-mediated interactions between mitochondrial ADP/ATP carrier monomers. *FEBS Lett* 579(27):6031-6036.
2. Pebay-Peyroula E*, et al.* (2003) Structure of mitochondrial ADP/ATP carrier in complex with carboxyatractyloside. *Nature* 426(6962):39-44.
3. Sanchez JF*, et al.* (2012) Unambiguous structure of atractyloside and carboxyatractyloside. *Bioorg Med Chem Lett* 22(8):2973-2975.
4. Macleod J, Gaul K, & Oelrichs P (1990) Bifloratoxin, a toxic aminoglycoside of carboxyatractyligenin, from *Melanthera biflora*. *Australian Journal of Chemistry* 43(9):1533-1539.
5. Kedrov A*, et al.* (2010) Probing the interactions of carboxy-atractyloside and atractyloside with the yeast mitochondrial ADP/ATP carrier. *Structure* 18(1):39-46.
6. Kolarov J, Kolarova N, & Nelson N (1990) A third ADP/ATP translocator gene in yeast. *J Biol Chem* 265(21):12711-12716.

7. Robinson AJ & Kunji ER (2006) Mitochondrial carriers in the cytoplasmic state have a common substrate binding site. *Proc Natl Acad Sci USA* 103(8):2617-2622.
8. Brandolin G, Meyer C, Defaye G, Vignais PM, & Vignais PV (1974) Partial purification of an atractyloside-binding protein from mitochondria. *FEBS Lett* 46(1):149-153.
9. Kunji ER & Crichton PG (2010) Mitochondrial carriers function as monomers. *Biochim Biophys Acta* 1797(6-7):817-831.
10. Hunte C*, et al.* (2005) Structure of a Na+/H+ antiporter and insights into mechanism of action and regulation by pH. *Nature* 435(7046):1197-1202.
11. Ressl S, Terwisscha van Scheltinga AC, Vonrhein C, Ott V, & Ziegler C (2009) Molecular basis of transport and regulation in the Na(+)/betaine symporter BetP. *Nature* 458(7234):47-52.
12. Yernool D, Boudker O, Jin Y, & Gouaux E (2004) Structure of a glutamate transporter homologue from Pyrococcus horikoshii. *Nature* 431(7010):811-818.
13. Bamber L, Harding M, Butler PJ, & Kunji ER (2006) Yeast mitochondrial ADP/ATP carriers are monomeric in detergents. *Proc Natl Acad Sci USA* 103(44):16224-16229.
14. Bamber L, Harding M, Monne M, Slotboom DJ, & Kunji ER (2007) The yeast mitochondrial ADP/ATP carrier functions as a monomer in mitochondrial membranes. *Proc Natl Acad Sci USA* 104(26):10830-10834.
15. Kunji ER & Harding M (2003) Projection structure of the atractyloside-inhibited mitochondrial ADP/ATP carrier of *Saccharomyces cerevisiae*. *J Biol Chem* 278(39):36985-36988.
16. Hashimoto M*, et al.* (1999) Expression of the bovine heart mitochondrial ADP/ATP carrier in yeast mitochondria: significantly enhanced expression by replacement of the N-terminal region of the bovine carrier by the corresponding regions of the yeast carriers. *Biochim Biophys Acta* 1409(3):113-124.
17. Crichton PG, Harding M, Ruprecht JJ, Lee Y, & Kunji ER (2013) Lipid, Detergent, and Coomassie Blue G-250 Affect the Migration of Small Membrane Proteins in Blue Native Gels: Mitochondrial Carriers Migrate As Monomers Not Dimers. *J Biol Chem* 288(30):22163-22173.
18. Flot D*, et al.* (2010) The ID23-2 structural biology microfocus beamline at the ESRF. *J Synchrotron Radiat* 17(1):107-118.
19. Battye TG, Kontogiannis L, Johnson O, Powell HR, & Leslie AG (2011) iMOSFLM: a new graphical interface for diffraction-image processing with MOSFLM. *Acta Crystallogr D Biol Crystallogr* 67(Pt 4):271-281.
20. Winn MD*, et al.* (2011) Overview of the CCP4 suite and current developments. *Acta Crystallogr D Biol Crystallogr* 67(Pt 4):235-242.
21. Kabsch W (2010) Xds. *Acta Crystallogr D Biol Crystallogr* 66(Pt 2):125-132.
22. Evans PR (2011) An introduction to data reduction: space-group determination, scaling and intensity statistics. *Acta Crystallogr D Biol Crystallogr* 67(Pt 4):282-292.
23. Evans P (2006) Scaling and assessment of data quality. *Acta Crystallogr D Biol Crystallogr* 62(Pt 1):72-82.
24. Adams PD*, et al.* (2010) PHENIX: a comprehensive Python-based system for macromolecular structure solution. *Acta Crystallogr D Biol Crystallogr* 66(Pt 2):213-221.

25. McCoy AJ*, et al.* (2007) Phaser crystallographic software. *J Appl Crystallogr* 40(Pt 4):658-674.
26. Emsley P, Lohkamp B, Scott WG, & Cowtan K (2010) Features and development of Coot. *Acta Crystallogr D Biol Crystallogr* 66(Pt 4):486-501.
27. Murshudov GN*, et al.* (2011) REFMAC5 for the refinement of macromolecular crystal structures. *Acta Crystallogr D Biol Crystallogr* 67(Pt 4):355-367.
28. Smart OS*, et al.* (2012) Exploiting structure similarity in refinement: automated NCS and target-structure restraints in BUSTER. *Acta Crystallogr D Biol Crystallogr* 68(Pt 4):368-380.
29. Winn MD, Isupov MN, & Murshudov GN (2001) Use of TLS parameters to model anisotropic displacements in macromolecular refinement. *Acta Crystallogr D Biol Crystallogr* 57(Pt 1):122-133.
30. Afonine PV*, et al.* (2012) Towards automated crystallographic structure refinement with phenix.refine. *Acta Crystallogr D Biol Crystallogr* 68(Pt 4):352-367.
31. Lebedev AA*, et al.* (2012) JLigand: a graphical tool for the CCP4 template-restraint library. *Acta Crystallogr D Biol Crystallogr* 68(Pt 4):431-440.
32. Schlame M (2008) Cardiolipin synthesis for the assembly of bacterial and mitochondrial membranes. *J Lipid Res* 49(8):1607-1620.
33. Ho SN, Hunt HD, Horton RM, Pullen JK, & Pease LR (1989) Site-directed mutagenesis by overlap extension using the polymerase chain reaction. *Gene* 77(1):51-59.
34. de Ruyter PG, Kuipers OP, & de Vos WM (1996) Controlled gene expression systems for *Lactococcus lactis* with the food-grade inducer nisin. *Appl Environ Microbiol* 62(10):3662-3667.
35. Monne M, Chan KW, Slotboom DJ, & Kunji ER (2005) Functional expression of eukaryotic membrane proteins in *Lactococcus lactis*. *Protein Sci* 14(12):3048-3056.
36. Laskowski RA & Swindells MB (2011) LigPlot+: multiple ligand-protein interaction diagrams for drug discovery. *J Chem Inf Model* 51(10):2778-2786.
37. Krissinel E (2012) Enhanced fold recognition using efficient short fragment clustering. *J MolBiochem* 1(2):76-85.

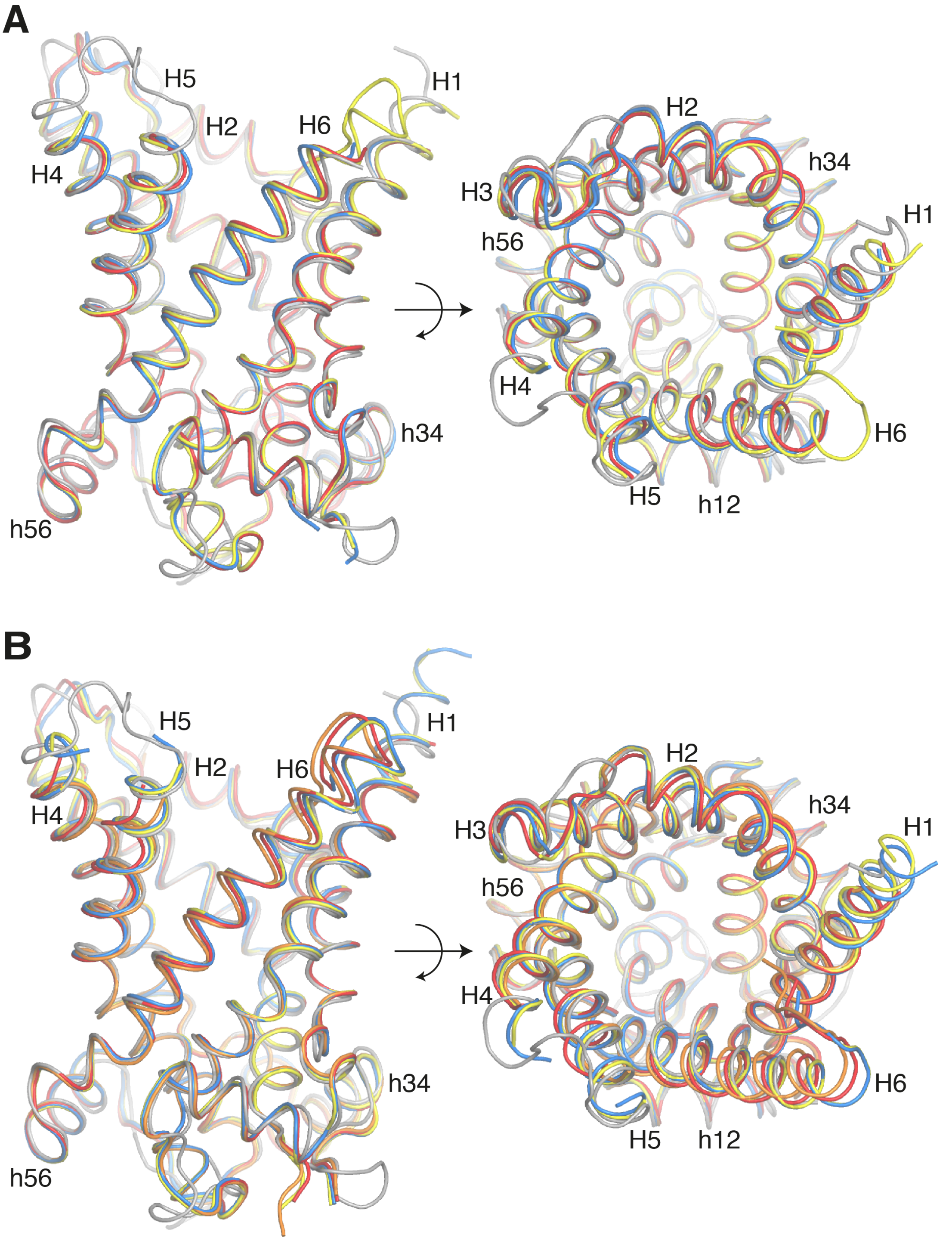

Figure S1: Superpositions of the structures of Aac2p (*A*) or Aac3p (*B*) and the bovine ADP/ATP carrier (pdb code 1OKC). In (*A*), 1OKC is shown in grey, the $C222_1$ Aac2p structure in red, and the $P2_12_12_1$ Aac2p structure in yellow (chain A) and blue (chain B). In (*B*), 1OKC is shown in grey, the $P2_12_12_1$ Aac3p structure in red (chain A) and orange (chain B), and the $P2_1$ structures in yellow (chain A) and blue (chain B). The structures are viewed from the plane of the membrane (left) and perpendicular to the membrane, from the cytoplasmic side (right).

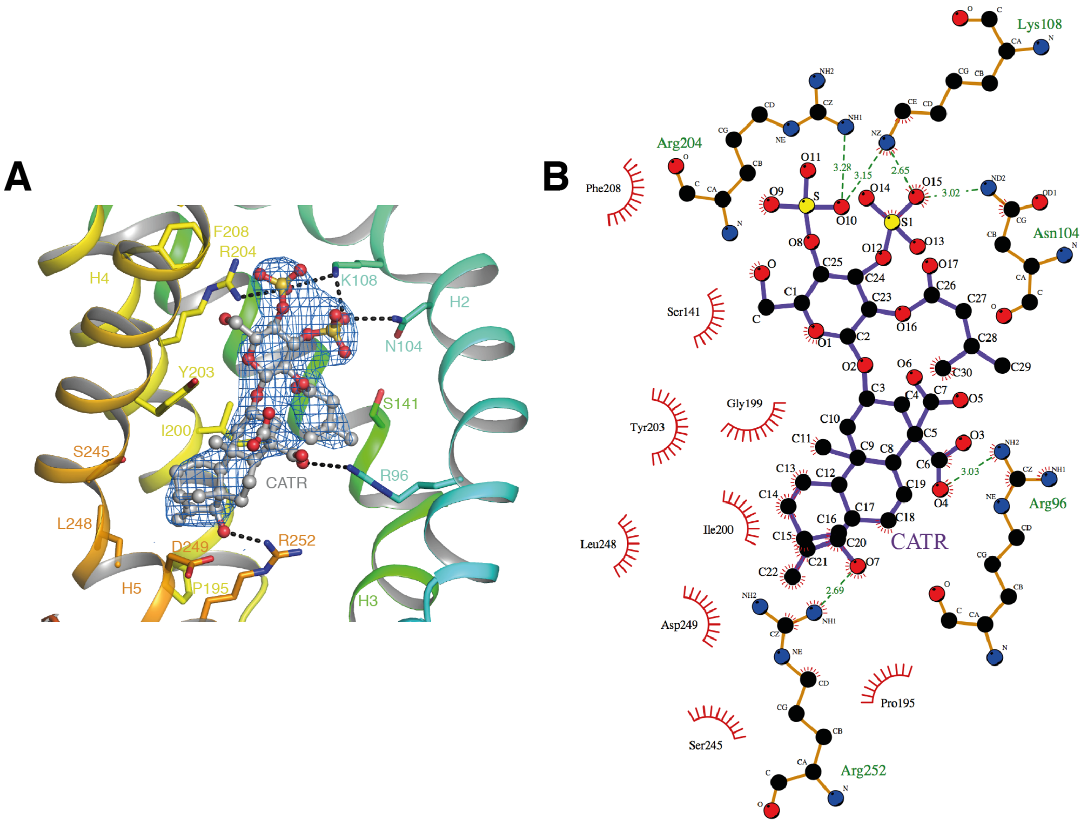

Figure S2: Architecture of the carboxyatractyloside binding-site. (*A*) The CATR binding-site in Aac2p (chain B of the $P2_12_12_1$ crystal form). CATR is shown in stick and sphere representation, with grey carbon atoms. Protein side chains interacting with the inhibitor are shown in stick representation and are labelled. Polar contacts between CATR and residues are shown as black dashed lines. H1 and H6 have been removed to allow a clearer view of the binding-site. The density, shown as a blue mesh, is a $2mF_o$-DF_c simulated annealing omit map, contoured at 1 σ, and displayed within 2 Å of the CATR molecule. Simulated annealing omit maps were obtained by omitting CATR coordinates before refinement in phenix.refine (24), using a starting temperature of 3000K for simulated annealing. (*B*) Ligplot diagram (36) of the CATR binding-site in Aac2p (chain B of the $P2_12_12_1$ crystal form). CATR bonds are shown in purple. Hydrogen bonds and salt bridges are shown as green dashed lines with indicated distances (Å). Red arcs indicate residues in hydrophobic contact with CATR with spokes radiating toward the CATR atoms they contact.

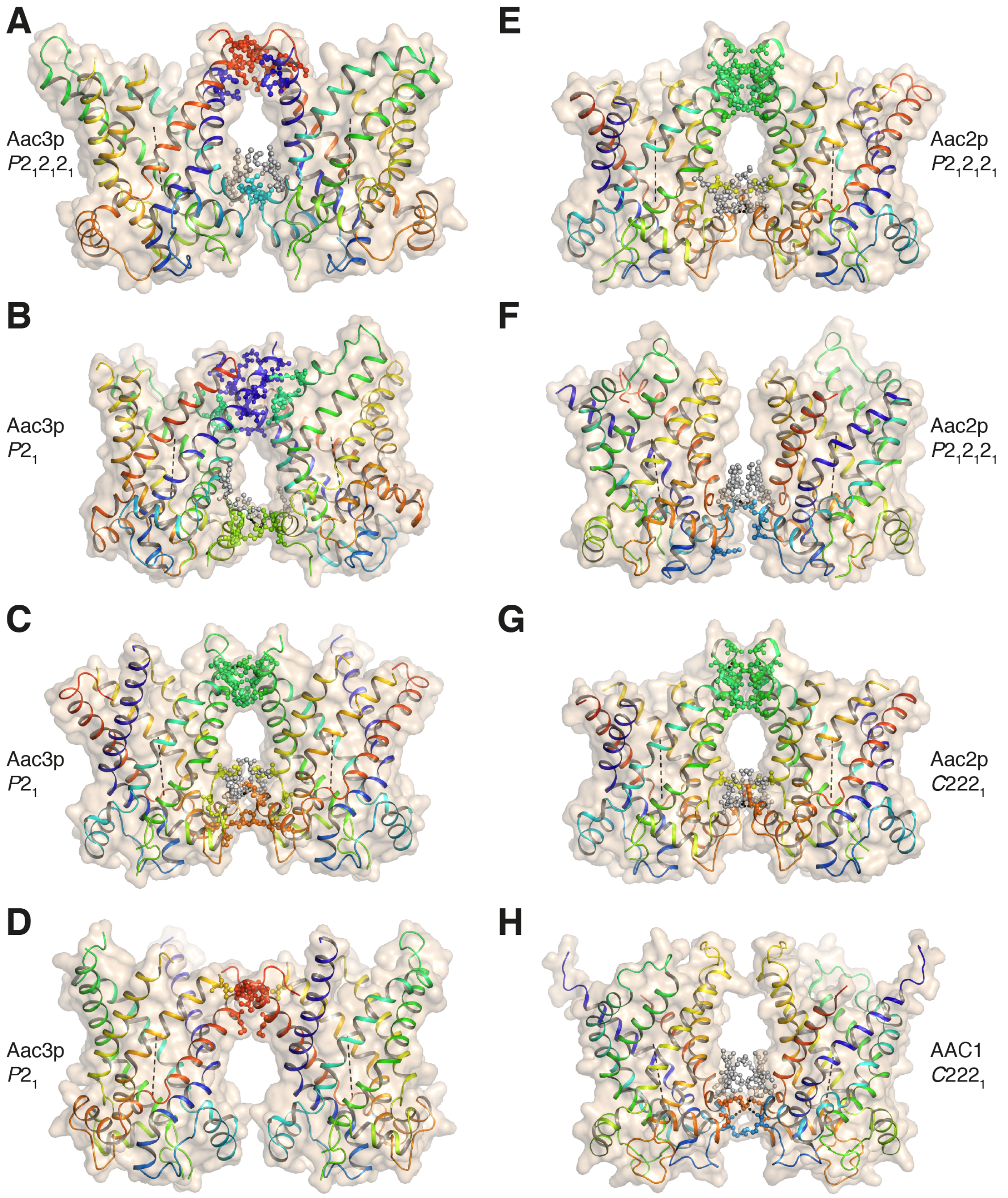

Figure S3: Interfaces between ADP/ATP carrier monomers in the different crystal forms. Lateral views of the interfaces are shown for the $P2_12_12_1$ Aac3p crystal (*A*), the $P2_1$ Aac3p crystal (*B*, *C*, *D*), the $P2_12_12_1$ Aac2p crystal (*E* and *F*), the $C222_1$ Aac2p crystal (*G*), and the bovine AAC1 $C222_1$ crystal (pdb code 2C3E) (*H*). The monomers are shown in rainbow colors (N-terminus in blue to C-terminus in red), and as a wheat-colored surface representation. Amino acid residues in close contact (4.5 Å or less apart) are shown in sphere and stick representation. Cardiolipin molecules involved in contacts are shown as grey-colored sticks and spheres. The 3-fold pseudo-symmetry axis for each monomer is shown as a black dashed line.

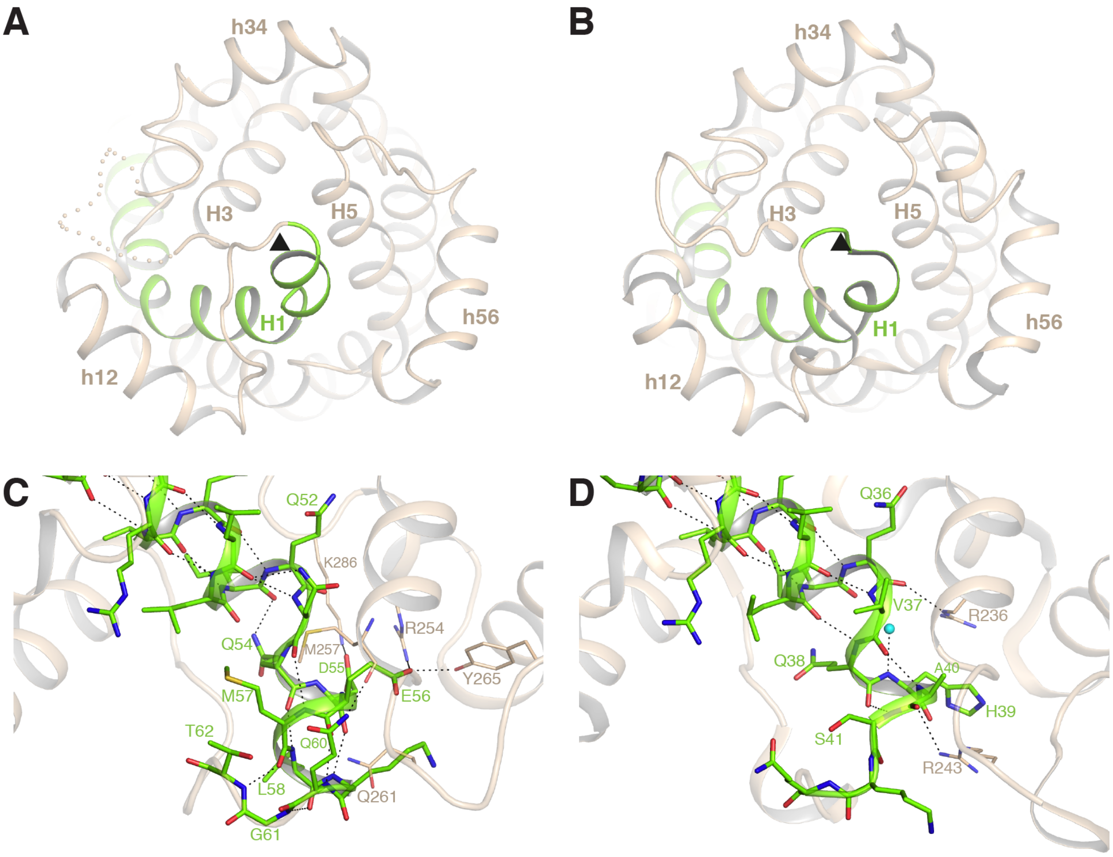

Figure S4: Positions of the matrix end of H1. (*A*) Matrix and (*C*) lateral views of the matrix side of H1 of Aac2p (chain A of the $P2_12_12_1$ crystal form). (*B*) and (*D*) Equivalent views of bovine AAC1 (PDB code 1OKC). H1 is highlighted in green, and the rest of the structure in wheat. Residues in H1 and its adjacent loop are shown in stick representation with green colored carbon atoms. In (*A*) and (*B*) a black triangle shows the three-fold pseudo-symmetry axis. In (*C*) and (*D*) neighboring residues that help stabilize the structures are shown as sticks with wheat carbons. A water molecule is shown as a cyan sphere in (*D*). Potential hydrogen bond and salt bridges are marked by black dotted lines. In (*C*) and (*D*), residues from H3 to H4 have been removed to enable a clearer view.

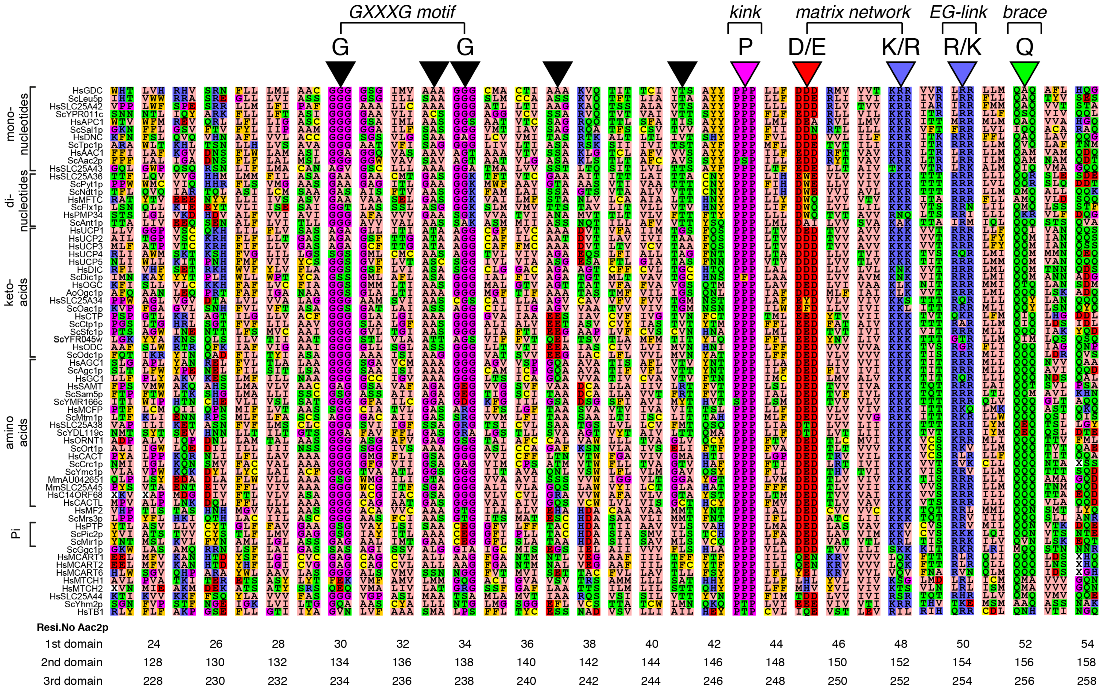

Figure S5: Equivalent residues of the odd-numbered α-helices in the three domains of mitochondrial carriers of *S. cerevisiae* (Sc) and *H. sapiens* (Hs), grouped together to emphasize the pseudo-symmetry in the three-fold repeat. Indicated are the residues involved in the GxxxG motif, the matrix salt bridge network, the kink, the brace and the EG-link, which consists of positively charged residues that often bind to the EG motif, located between the matrix and linker helices. Amino acids are colored according to their properties: basic residues are blue, acidic red, polar green, aliphatic pink, aromatic orange, Gly and Pro magenta, and Cys yellow. The even residue numbers of Aac2p are shown below.

Table S1: Data collection and refinement statistics

	Aac2p	Aac2p	Aac3p	Aac3p
Data collection				
Space group	$C222_1$	$P2_12_12_1$	$P2_1$	$P2_12_12_1$
Cell dimensions				
a, *b*, *c* (Å)	66.9, 105.7, 98.6	67.4, 98.2, 105.1	56.7, 107.9, 57.0	40.3, 104.2, 154.1
α, β, γ (°)	90, 90, 90	90, 90, 90	90, 93.6, 90	90, 90, 90
Resolution (Å)	36.05-2.49 (2.62-2.49)	19.84-3.20 (3.46-3.20)	41.45-3.20 (3.42-3.20)	49.34-3.40 (3.67-3.40)
R_{merge}	0.094 (0.905)	0.194 (0.612)	0.133 (0.412)	0.252 (0.718)
R_{pim}	0.043 (0.409)	0.118 (0.369)	0.112 (0.349)	0.144 (0.410)
CC(1/2)	0.996 (0.714)	0.982 (0.759)	0.987 (0.829)	0.975 (0.674)
$<<I>/\sigma<I>>$	10.3 (2.1)	6.9 (2.4)	5.7 (2.5)	5.9 (2.1)
Completeness (%)	99.9 (99.8)	99.5 (99.9)	98.0 (98.3)	99.2 (96.6)
Redundancy	5.7 (5.7)	3.6 (3.7)	2.1 (2.1)	3.9 (4.0)
No. molecules/asu[†]	1	2	2	2
No. asu/unit cell	8	4	2	4
Refinement				
Resolution (Å)	36.05-2.49	19.84-3.20	41.45-3.20	38.98-3.40
No. reflections	12532	11888	11083	9415
R_{work} (%)	25.90	24.91	25.78	24.95
R_{free} (%)	29.73	28.04	29.48	29.69
No. atoms	2160	4475	4576	4413
Protein	1985	4110	4259	4067
Ligand	175	365	317	346
Water	0	0	0	0
Mean *B*-factors	78.40	30.80	29.40	61.20
Protein	78.10	30.40	28.90	60.70
Ligand/ion	82.40	35.00	36.20	67.50
R.m.s. deviations				
Bond lengths (Å)	0.003	0.003	0.002	0.002
Bond angles (°)	0.91	0.83	0.77	0.83
Molprobity clashscore	4.74	3.53	4.14	3.01
Molprobity Ramachandran analysis: favoured/allowed/outliers (%)	99.61/0.39/0.00	99.63/0.37/0.00	99.29/0.71/0.00	98.11/1.89/0.00

*Values in parentheses are for highest-resolution shell.

[†] asu: asymmetric unit

Table S2: Root mean square deviations after superposition of ADP/ATP carrier structures. Structure RMSDs were calculated using Gesamt (37).

Structure aligned to 1OKC	RMSD (Å)	Number of aligned residues
2C3E	0.73	289
$C222_1$ Aac2p	0.93	258
$P2_12_12_1$ Aac2p chain A	0.92	262
$P2_12_12_1$ Aac2p chain B	0.91	259
$P2_1$ Aac3p chain A	0.89	270
$P2_1$ Aac3p chain B	0.94	271
$P2_12_12_1$ Aac3p chain A	0.92	263
$P2_12_12_1$ Aac3p chain B	0.89	252

Table S3: Direct protein-carboxyatractyloside interactions observed in crystal structures of ADP/ATP carriers. Protein-ligand interactions were analysed using LigPlot+ (36).

Interaction	Protein:CATR atom*	Interaction distance (Å)									
		S. cerevisiae Aac2p			*S. cerevisiae* Aac3p				*B. taurus* AAC1		
		$C222_1$	$P2_12_12_1$		$P2_12_12_1$		$P2_1$		$P2_12_12$ (1OKC)	$P2_12_12$ (Sanchez et al. remodelling)	$C222_1$ (2C3E)
			A	B	A	B	A	B			
Salt-bridge	Arg204:Sulfate O9/O10/O11	3.2	3.1	3.3	3.4	3.4	2.8	2.9	3.1	3.3	3.2
Salt-bridge	Lys108:Sulfate O9/O10/O11	3.4	2.9	3.2	3.1	3.2	2.6	2.5	2.9	2.8	3.1
Salt-bridge	Lys108:Sulfate O14/O15	3.1	2.7	2.7	3.1	3.4	3.0	2.9	2.7	2.7	3.3
Hydrogen-bond	Asn104:Sulfate O15			3.0	2.3	2.7	2.9	2.9	2.9	3.0	
Salt-bridge	Arg96:Carboxylate O3/O4	2.7	3.2	3.0	3.2	2.9	3.1	2.9	2.6	2.6	3.2
Hydrogen-bond	Arg252:Hydroxyl O7	2.8	2.7	2.7	2.7	2.4	2.6	2.6	3.0	2.9	
Non-bonded contacts		Ser141 Gly199 Tyr203 Phe208 Ser245 Leu248 Asp249 Arg253	Gly138 Ser141 Gly199 Ile200 Tyr203 Phe208 Ser245 Asp249	Ser141 Pro195 Gly199 Ile200 Tyr203 Phe208 Ser245 Leu248 Asp249	Ser130 Gly188 Ile189 Tyr192 Ser234 Asp238 Arg242	Ser130 Leu131 Gly188 Tyr192 Phe197 Ser234 Leu237 Asp238 Arg242	Pro184 Gly188 Ile189 Tyr192 Phe197 Ser234 Leu237 Asp238	Ser130 Pro184 Gly188 Ile189 Tyr192 Phe197 Ser234 Leu237 Asp238	Gly123 Leu127 Gly182 Ile183 Tyr186 Ser227 Phe230 Asp231 Arg235	Gly123 Leu127 Gly182 Ile183 Tyr186 Ser227 Phe230 Asp231 Arg235	Gly123 Ser126 Leu127 Gly182 Ile183 Tyr186 Ser227 Phe230 Asp231 Arg234

*Protein residue labelling is based on the *S. cerevisiae* Aac2p sequence (except for the non-bonded contacts). CATR atom labelling is shown in Figure S2.

Table S4: Protein-cardiolipin interactions observed in crystal structures of ADP/ATP carriers. Protein-ligand interactions were analysed using LigPlot+ (36).

Lipid	Interaction	Protein residue involved (interaction distance, Å)								
		S. cerevisiae Aac2p			*S. cerevisiae* Aac3p				*B. taurus* AAC1	
		$C222_1$	$P2_12_12_1$		$P2_12_12_1$		$P2_1$		$P2_12_12$ (1OKC)*	$C222_1$ (2C3E)
			A	B	A	B	A	B		
Cdl800	Linker helix amide:phosphate	Gly89 (2.9)	Gly89 (3.1)	Gly89 (3.0)	Gly78 (2.6)	Gly78 (3.1)	Gly78 (2.3)	Gly78 (2.9)	Gly72 (2.5)	Gly72 (2.5)
	Helix 2 N-terminal amide:phosphate	Thr91 (2.8)	Thr91 (3.1)	Thr91 (3.0)	Thr80 (3.3)	Thr80 (3.3)	Thr80 (2.3)	Thr80 (3.1)	Leu74 (2.8)	Leu74 (3.3)
	Matrix helix h34 N-terminal amide:phosphate	Leu173 (3.3) Ile174 (3.4)	Ile174 (3.5)	Ile174 (3.4)	Thr163 (3.4)	Leu162 (3.0)	Thr163 (3.3)	Thr163 (2.7)		Leu156 (3.3) Gly157 (3.1) Asn158 (3.3)
	Side chain:phosphatidyl oxygen	Asn90 (3.0)	Asn90 (2.6)							
	Side chain:phosphate				Thr80 (2.8) Thr163 (2.7)	Thr80 (2.8) Thr163 (2.8)				
	Hydrophobic contacts	Trp87 Arg88 Leu173 Ile174	Trp87 Arg88 Gly172 Leu173 Ile174	Trp87 Arg88 Asn90 Leu173 Ile174	Trp76 Arg77 Gly78 Gly161 Leu162	Trp76 Arg77 Gly78 Gly161	Trp76 Arg77 Asn79 Val83 Gly161 Leu162	Trp76 Arg77 Asn79 Val83 Gly161 Leu162	Thr23 Trp70 Arg71 Asn73 Val77 Leu140 Gly155 Leu156	Val16 Ala19 Thr23 Trp70 Arg71 Val77 Pro82 Phe81 Gly155
Cdl801	Linker helix amide:phosphate	Gly287 (2.5)	Gly287 (2.6)	Gly287 (2.6)	Gly276 (2.9)	Gly276 (3.2)	Gly276 (2.8)	Gly276 (2.6)	Gly272 (2.7)	Gly272 (2.4)
	Helix 6 N-terminal amide:phosphate	Gly289 (2.7) Ala290 (3.4)	Gly289 (2.9)	Gly289 (2.8) Ala290 (3.2)	Gly278 (3.4)	Gly278 (2.9)	Gly278 (3.2)	Gly278 (3.2)	Trp274 (3.1) Ser275 (3.0)	Trp274 (2.6) Ser275 (3.0)
	Matrix helix h12	Ile70 (3.1)	Ile70 (3.2)	Ile70 (3.0)	Ile59 (3.1)	Ile59 (3.0)	Ile59 (3.2)	Ile59 (3.1)	Ile53 (3.3)	Ile53 (3.0)

	N-terminal amide:phosphate		Leu71 (3.2)	Leu71 (3.2)	Val60 (3.0)	Val60 (3.2)	Val60 (3.1)	Val60 (3.2)	Ile54 (2.9)	Ile54 (2.8)
	Side chain:phosphatidyl oxygen									
	Side chain:phosphate								Ser275 (3.1)	
	Hydrophobic contacts	Ile51 Gly69 Leu71 Phe285 Lys286 Cys288 Ile292 Leu293	Ile51 Gly69 Phe285 Lys286 Cys288	Ile51 Gly69 Phe285 Lys286 Cys288 Ile292 Leu293	Ile40 Gly58 Phe274 Gly278 Ile281 Leu282	Gly58 Phe274 Cys277 Ile281 Leu282	Ile40 Gly58 Thr232 Phe274 Lys275 Cys277 Ile281	Ile40 Gly58 Gly229 Thr232 Phe274 Lys275 Cys277 Ile281	Leu35 Gly52 Leu225 Phe270 Lys271 Leu278	Leu35 Gly52 Leu225 Phe270 Lys271 Ala273
Cdl802	Linker helix amide:phosphate	Gly192 (2.6)	Gly192 (3.0)	Gly192 (2.6)	Gly181 (3.0)	Gly181 (3.2)	Gly181 (3.2)	Gly181 (2.7)		Gly175 (3.1)
	Helix 4 N-terminal amide:phosphate	Phe193 (3.3)	Phe193 (3.4)		Met183 (3.0)	Met183 (2.9)				Asn177 (3.3)
	Matrix helix h56 N-terminal amide:phosphate	Ala268 (2.8) Phe269 (2.9)	Ala268 (2.7) Phe269 (2.9)	Ala268 (2.7) Phe269 (3.1)	Ala257 (3.3) Ile258 (3.1)	Ala257 (3.3) Ile258 (3.2)	Ala257 (2.6) Ile258 (3.3)	Ala257 (2.9) Ile258 (3.0)		Thr253 (2.9) Val254 (3.3)
	Side chain:phosphatidyl oxygen									Asn177 (2.7)
	Side chain:phosphate						Arg180 (3.3)			Thr253 (3.0)
	Hydrophobic contacts	Tyr190 Arg191 Leu194 Val198 Leu248 Met255 Gly267	Leu143 Tyr190 Arg191 Leu194 Val198 Leu248 Gly267	Leu143 Phe144 Ala187 Tyr190 Arg191 Leu194 Val198 Leu248	Phe116 Leu132 Ile175 Ala176 Tyr179 Arg180 Val187 Leu237	Leu132 Ile175 Ala176 Tyr179 Phe182 Pro184 Leu237 Gly256	Ile175 Ala176 Tyr179 Phe182 Met183 Pro184 Val187 Leu237	Ile175 Ala176 Tyr179 Arg180 Phe182 Met183 Val187 Leu237	Cys128 Tyr173 Phe176 Asn177 Val180 Gln181	Tyr94 Thr125 Cys128 Phe129 Gln174 Phe176 Gln181 Gly252

				Met255 Gly267	Met244 Gly256		Met244 Gly256 Ile258	Met244 Gly256 Ile258		

*In 1OKC, cardiolipins 800 and 802 show unusual structures. Cdl800 folds back on itself, allowing only one phosphate to interact with the protein (the linker helix Gly and helix 2 dipole). A phosphatidylcholine lipid molecule has been modelled close to cdl800, and appears to interact with the dipole and amide groups of matrix helix h34. Only part of cdl802 is modelled (one phosphatidyl moiety), and it is displaced from the position of equivalent groups in the other structures.

Table S5: Intra-domain and inter-domain polar interactions observed in crystal structures of ADP/ATP carriers

For this analysis, we have included all interactions between residues up to 3.5 Å apart having reasonable geometry.

Interaction type	Distance, d (Å)	Number of interactions						
		S. cerevisiae Aac2p			*S. cerevisiae* Aac3p		*B. taurus* AAC1	
		$C222_1$	$P2_12_12_1$ chain A	$P2_12_12_1$ chain B	$P2_1$ chain A	$P2_1$ chain B	$P2_12_12$ (1OKC)*	$C222_1$ (2C3E)*
Intra-domain	$d \leq 2.8$	4	5	5	3	3	7	5
	$2.8 < d \leq 3.2$	12	9	11	3	3	12	7
	$3.2 < d \leq 3.5$	1	7	5	8	6	0	0
	Total	17	21	21	14	12	19	12
Inter-domain	$d \leq 2.8$	5	1	3	3	3	5	4
	$2.8 < d \leq 3.2$	5	8	7	5	4	5	2
	$3.2 < d \leq 3.5$	6	3	2	5	5	0	0
	Total	16	12	12	13	12	10	6

* The side chain of Gln36 in AAC1, equivalent to Gln52 in Aac2p, has been rotated by 180° for this analysis.